

Bulk stress distributions in the pore space of sphere-packed beds under Darcy flow conditionsNgoc H. Pham,¹ Roman S. Voronov,² Naga Rajesh Tummala,^{1,*} and Dimitrios V. Papavassiliou^{1,†}¹*School of Chemical, Biological, and Materials Engineering, University of Oklahoma, Norman, Oklahoma 73019-1004, USA*²*Department of Chemical Biological and Pharmaceutical Engineering, New Jersey Institute of Technology—University Heights, Newark, New Jersey 07102, USA*

(Received 14 August 2013; revised manuscript received 8 February 2014; published 26 March 2014)

In this paper, bulk stress distributions in the pore space of columns packed with spheres are numerically computed with lattice Boltzmann simulations. Three different ideally packed and one randomly packed configuration of the columns are considered under Darcy flow conditions. The stress distributions change when the packing type changes. In the Darcy regime, the normalized stress distribution for a particular packing type is independent of the pressure difference that drives the flow and presents a common pattern. The three parameter (3P) log-normal distribution is found to describe the stress distributions in the randomly packed beds within statistical accuracy. In addition, the 3P log-normal distribution is still valid when highly porous scaffold geometries rather than sphere beds are examined. It is also shown that the 3P log-normal distribution can describe the bulk stress distribution in consolidated reservoir rocks like Berea sandstone.

DOI: [10.1103/PhysRevE.89.033016](https://doi.org/10.1103/PhysRevE.89.033016)

PACS number(s): 47.56.+r, 83.10.-y, 47.11.-j

I. INTRODUCTION

Motion of colloidal particles, microparticles and nanoparticles through porous media has been found to be important in many engineering disciplines such as tissue engineering, environmental engineering, and petroleum engineering. In tissue engineering, deposition of biocolloids (cells) on the surface of a porous scaffold and cell proliferation is a desired process. This process is strongly affected by the flow-induced stresses that can either enhance the attachment of the suspended particles to the pore surfaces or wash attached particles away from the surfaces [1–4]. In environmental applications, nanoparticles released to the subsurface during the disposal of nanomaterials might penetrate the soil and contaminate the water table and aquifers. Several types of nanoparticles have been reported to be toxic to many animal species and humans [5–11]. In petroleum engineering, the evolution of nanomaterials has opened up an opportunity for developing nanosensors that can be helpful in enhanced oil recovery (EOR) [12–15]. Those nanoparticles should be specifically fabricated so they can propagate through the reservoir rock. By measuring their responses to external signals, detailed information about the reservoir can be obtained [12–15]. In addition, surfactant-based EOR depends on the stability of colloidal particles propagating through a hydrocarbon reservoir [16], while the self-assembly of surfactants into micelles is strongly sensitive to flow-induced shear stresses [17,18].

The stability and mobility of micro- and nanoparticles in the above scenarios depend on flow-induced stresses. These stresses can cause aggregation of nanoparticles and micelles and, in turn, result in sedimentation or size exclusion of large particles, while moving through the pores [17,19–23]. These are unwanted phenomena in applications where suspension stability, mobility, and long travel distance of nanoparticles are crucial prerequisites (e.g., EOR). It is therefore important

to either predict or measure the stress distribution in the flow field occurring in a porous material when releasing particles into that field. Unfortunately, knowing how stresses distribute from experimental measurements is a cumbersome task [24]. On the other hand, simulation results have been recently obtained that present the distribution of flow-induced stresses on the fluid-solid interface in the pore space of media with different geometric configurations, ranging from fiber webs to packed beds [25–33]. Based on such results, a common three-parameter (3P) γ distribution describing normalized surface stress distributions has been proposed [30]. While a lot of attention has focused on surface stresses, neither simulation models nor mathematic models address how bulk stresses distribute in the open pore spaces of the geometry. This is critical, because particles in stable suspensions might not settle on the solid surfaces, but instead they might be anywhere in the geometry. As stated earlier, this is especially important for those processes that require particles of high mobility that do not deposit and do not aggregate.

In this work, normalized stress distributions inside the open spaces (in the bulk of the fluid) of ideally packed beds with spherical beads [i.e., face centered cubic (fcc), body centered cubic (bcc), simple cubic (sc), and random packing], consolidated Berea sandstone, and structured fiber-web geometries were numerically investigated. The contributions of this paper are to (a) examine whether the stress distributions can be described by a common form of a probability density function (pdf); (b) explore the physical reason behind the observation of a common pdf, if it exists; and (c) determine how the stresses within the open space of porous media can be theoretically predicted.

II. NUMERICAL METHOD AND SIMULATION SETUP**A. Lattice Boltzmann method**

The lattice Boltzmann method (LBM) used herein is for a single phase, Newtonian, and incompressible fluid. In the lattice Boltzmann algorithm, the discrete Boltzmann equation is solved iteratively given the number of directions in space, m ,

*Currently at the School of Chemistry and Biochemistry at Georgia Institute of Technology.

†Corresponding author: Fax: (405) 325-5813, dvpapava@ou.edu

and the number of velocity lattice vectors, n (usually denoted as $DmQn$) [34,35]. In this study, the D3Q15 LBM is employed. The fluid flow is simulated by calculating the collisions and interactions between fluid particles that move on a uniform rectangular lattice. The fluid particles undergo three steps: propagation, collision, and forcing, that are modeled by the change of the particle distribution function at every time step as follows:

$$\underbrace{f_i(\vec{x} + \vec{e}_i \Delta t, t + \Delta t)}_{\text{STREAMING}} = \underbrace{f_i(\vec{x}, t)}_{\text{COLLISION}} \pm \underbrace{\mathcal{F}_i}_{\text{FORCING}}, \quad (1)$$

where f is the particle distribution function, \vec{x} is position, t is time, Δt is the time step, \vec{e} is the lattice velocity, Ω is the collision operator, \mathcal{F} is the forcing factor (pressure drop over length), and the subscript “ i ” is the lattice direction index, taking values from 0 to $n - 1$. The single relation time approximation model of Bhatnagar-Gross-Krook (BGK model) is used to characterize the particle-particle collision [35],

$$\Omega_i(\vec{x}, t) = -\frac{1}{\kappa} (f_i - f_i^{\text{eq}}), \quad (2)$$

where f^{eq} is the particle equilibrium distribution function and is given as

$$f_i^{\text{eq}}(\vec{x}) = w_i \rho \left[1 + 3 \frac{\vec{e}_i \cdot \vec{U}}{c^2} + 9 \frac{(\vec{e}_i \cdot \vec{U})^2}{c^4} - \frac{3 \vec{U}^2}{2 c^2} \right], \quad (3)$$

where $c = \frac{\Delta x}{\Delta t}$ is the lattice speed, Δx is the lattice constant, w is a lattice specific weighing factor, and U is the macroscopic velocity. The time κ appearing in Eq. (2) is the time scale with which the local particle distribution function relaxes to equilibrium and is often referred to as the relaxation time. It is related to the kinematic viscosity, ν , of the fluid as follows:

$$\nu = \frac{1}{3} \left(\kappa - \frac{1}{2} \right). \quad (4)$$

No slip boundary condition at the wall is achieved by applying the half-way bounce back technique, in which a particle will return to its original position with opposite direction if it hits the wall [34]. Conservation of mass and momentum allows the calculation of macroscopic properties (i.e., fluid density, ρ , and flow velocity, U) from discrete microscopic properties (f_i and e_i)

$$\rho = \sum_{i=0}^{n-1} f_i, \quad (5)$$

$$\rho \vec{U} = \sum_{i=0}^{n-1} f_i \vec{e}_i, \quad (6)$$

where n is the number of allowable directions that the fluid particles are allowed to move, including the zero position (the rest node). Our algorithm has been previously validated for use in porous media [30,36,37].

B. Simulation setup

Stress distributions in the open spaces of ideally packed spheres (sc, bcc, and fcc) and randomly packed spheres were mainly investigated. Among these, the random sphere packing was created by using event-driven molecular dynamics and

a modified Lubachevsky-Stillinger algorithm [38]. Packed spheres were rigid, impermeable, and 1 mm in diameter. To simulate an infinite array of spheres, periodic boundary conditions were applied in the three space directions, X, Y, and Z. In addition, other porous media configurations that may be found to describe synthetic scaffold geometries that are structured were generated. In biomedical applications, like tissue engineering, porous scaffolds serve as three-dimensional structures on which seeded stem cells can attach, proliferate, and finally form three-dimensional (3D) extracellular matrix producing functional tissue for transplantation. It has been found that all of these processes are promoted by flow-induced stresses, so flow perfusion bioreactors are often used for the dynamic culturing of the cell-seeded scaffolds [32,39–42]. These cases were analyzed using commercial, finite volume-based computational fluid dynamics (CFD) software [43–45].

Furthermore, the stress distribution within the pore space of a consolidated reservoir rock, in this case Berea sandstone, was also computed with LBM. The digital 3D geometry of the Berea rock sample was reconstructed from micro-computed tomography (μ CT) images obtained by use of an Xradia MicroXCT 400 machine. Over 900 grayscale images, each representing a slice of the rock, were taken with a resolution of 4.5 μ m. These images were then converted into binary images with only two intensities, 0 and 1, containing information of either empty nodes or solid nodes, and reattached to form virtual 3D geometry by a custom-written code in MATLAB. A thin slab of the virtual 3D geometry was used as the representative elementary volume of the porous medium.

Details of the geometry characteristics and the flow conditions of all studied cases are summarized in Table I. An incompressible and Newtonian fluid with a viscosity of 0.001 Pa s, which is equivalent to that of water, was employed as the working fluid. Three different pressure drop values of 10, 100, and 1000 Pa/m were applied for all the sphere-packing cases. A pressure drop of 100 000 Pa/m was used for flow in the six porous scaffolds and a pressure drop of 10 000 Pa/m was used for flow in the Berea sandstone.

The flow-induced stress tensor $\underline{\underline{\tau}}$ was calculated from the rate of strain as follows:

$$\underline{\underline{\tau}} = \frac{1}{2} \eta (\nabla \underline{U} + \nabla \underline{U}^T), \quad (7)$$

where η is the dynamic viscosity of the fluid and U is the velocity vector. The largest eigenvalue of this tensor was then considered to be the most important flow-induced stress, as previously done in Porter *et al.* [46] and in prior work in our laboratory [35]. The calculation of the pdf of the fluid stresses in the open spaces excluded the surface stresses on the fluid-solid interfaces. The stresses obtained from Eq. (7) were then normalized by subtracting the mean stress, $\bar{\tau}$, and dividing by the standard deviation, σ_τ , of the stress distribution as follows:

$$\tau^* = \frac{(\tau - \bar{\tau})}{\sigma_\tau}. \quad (8)$$

Note that this dimensionless variable is defined similarly to the random variable of the standard normal distribution (in that case the variable has a mean of zero and a standard deviation equal to 1). It is justified to use this normalization here, since

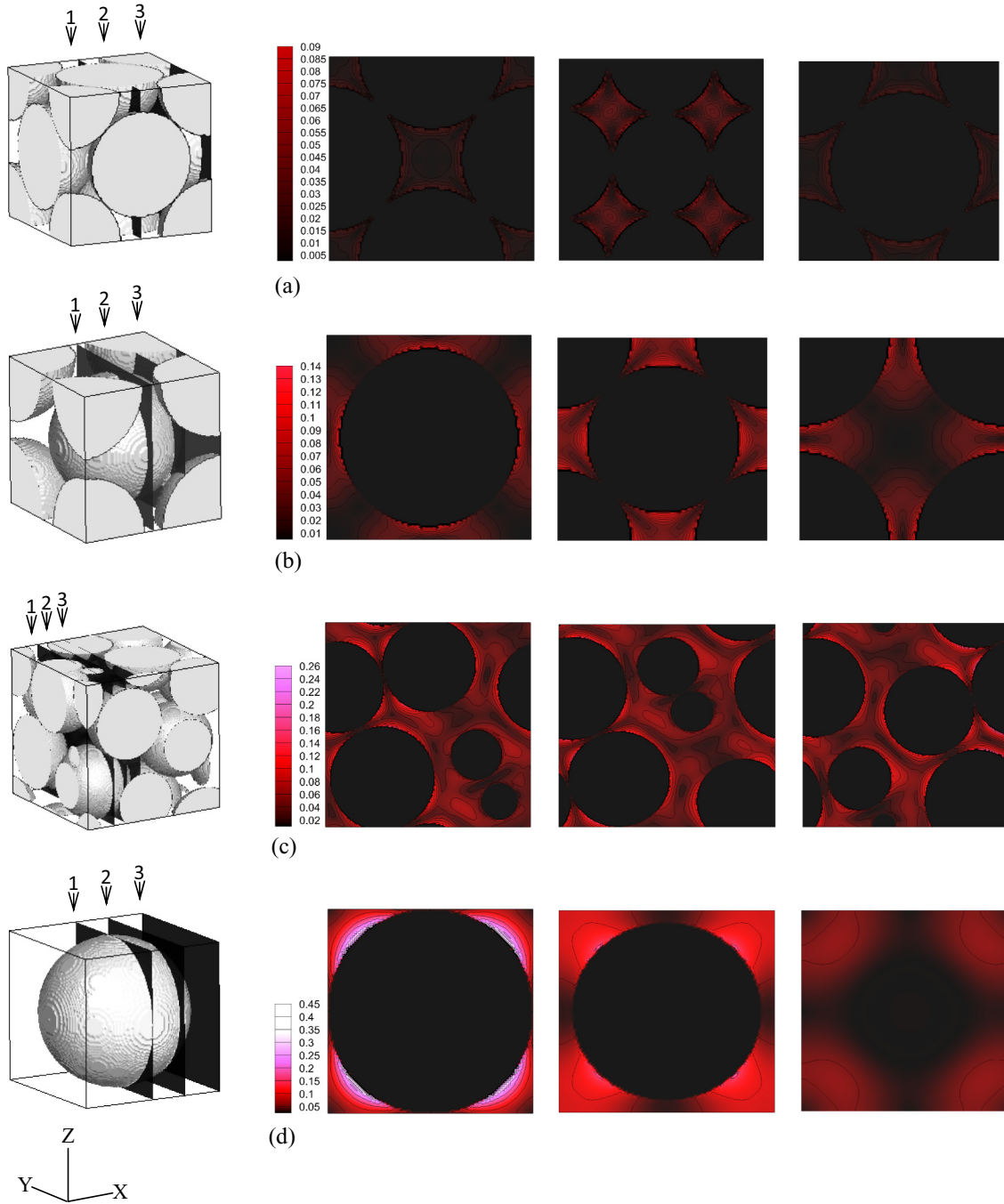


FIG. 1. (Color online) Contours of stresses in the open pore space for different sphere packing geometries. Stresses at three different positions, marked by 1, 2, and 3 are shown in slices from left to right. The units of the color scale bar are in $\text{g/cm}^2 \text{s}^2$. This is the case when a pressure drop of 100 Pa/m is employed. Spheres in (a) fcc packing, (b) bcc packing, (c) random packing, and (d) sc packing are shown.

we want to obtain a general form of the stresses that can be applicable in different porous media geometries rather than a case-specific distribution. The obtained dimensionless stresses were then partitioned into 100 bins of equal width, and the stress pdf was calculated by dividing the fractional occurrence of normalized stresses in a particular bin by the width of that bin. A Kolmogorov-Smirnov (KS) goodness-of-fit test, conducted using the software EASYFIT version 5.4 [47], was used to examine whether the stress pdf followed a known form of pdf.

III. RESULTS AND DISCUSSION

A. Distributions of dimensional and normalized stresses in columns packed with spheres

In Fig. 1 we plot four different geometries of sphere packings with contours of the associated stresses in the pore space. In each case, the contours of the pore stresses in three different planes that are perpendicular to the flow direction are shown. It can be seen from the color maps in Fig. 1 that stresses in the low range are dominant. In fcc and randomly

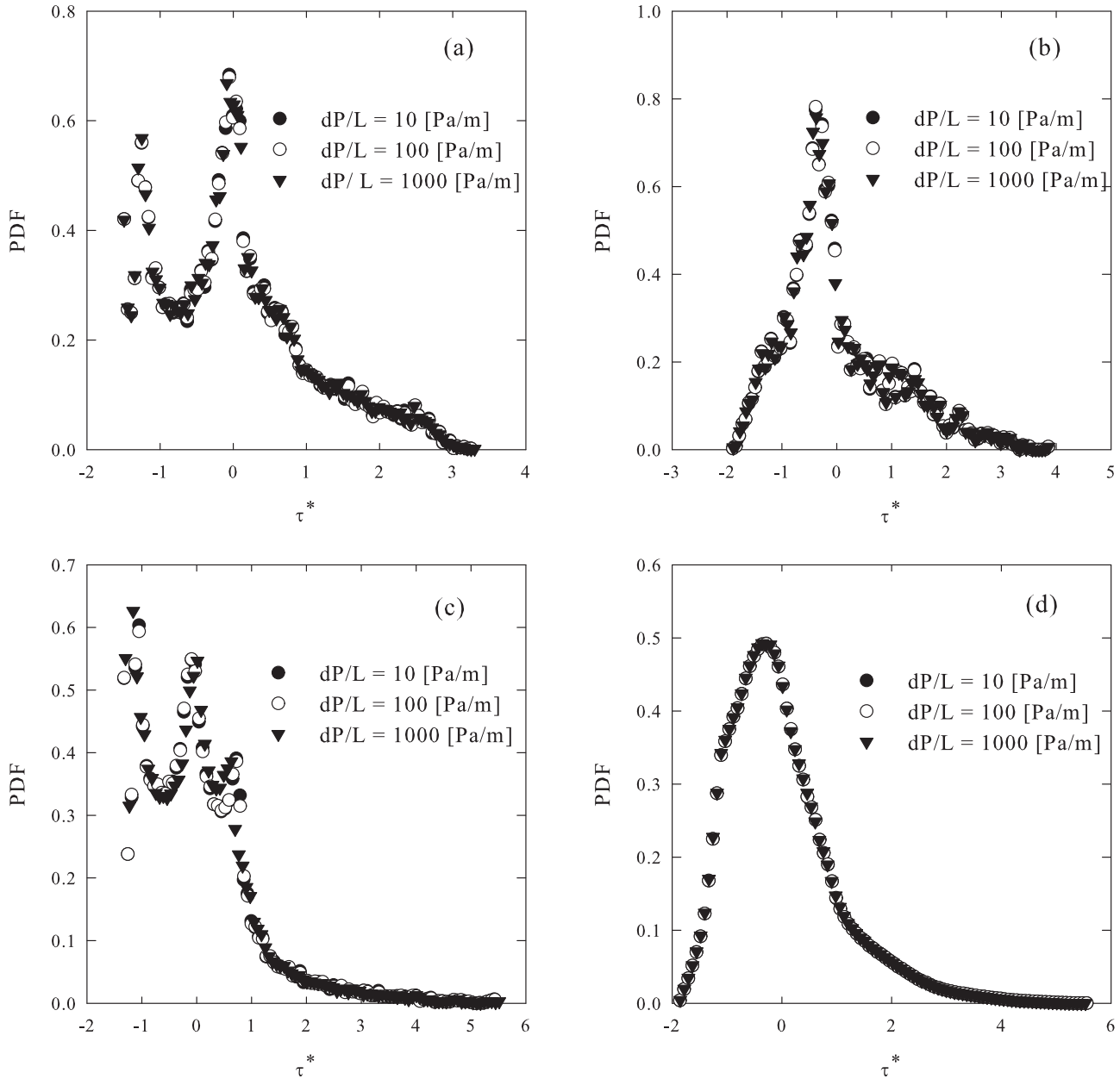


FIG. 2. Normalized stress distributions of four tested sphere packing types at three different pressure drop values. Spheres are packed in (a) bcc, (b) fcc, (c) sc, and (d) random configurations. Under Darcy flow conditions, the pattern of the distribution in each particular sphere geometry is unchanged.

packed spheres, it seems like there are large areas with low stresses and small areas of high stresses. On the other hand, in the bcc and sc sphere-packing cases, the low stresses and the high stresses cover almost equal areas.

Figure 2 is a presentation of the stress distributions in dimensionless form of the four sphere-packing types at three different pressure drops in the Darcy flow regime. The stress data were normalized by utilizing Eq. (8). A common feature in all the distributions observed in Fig. 2 is the positive skewness, i.e., the tail of the (pdf) to the right is longer. It is also seen that the normalized stress distribution corresponding to each particular configuration of packed spheres is characteristic to that specific configuration, i.e., the fcc packing and the random packing result in distributions with a single mode, whereas

those of the bcc packing and the sc packing are bimodal and trimodal, respectively. Knowing this distribution is critical to quantitatively predict the probability of finding a certain range of stresses in the flow field. When the dimensional mean stress and the standard deviation of the stress pdf are known, then obtaining a dimensional stress distribution from a normalized one is straightforward. The difference in the number of modes might be attributed to the nonuniformity of the pore sizes, in the sense that a continuous pore size distribution without modes leads to a bulk stress distribution with a single mode (see Fig. 8 in the appendix for the pore size distributions of the four sphere packing types). By that logic, the multiple modes of the bcc and sc sphere packing are expected, because the pore size distribution in these cases is multimodal and can be represented

with capillary tubes with distinct but almost uniform diameters. Although the shape of these distributions differs from packing to packing, there is no change in their shape when a particular type of packing undergoes different pressure drops, because of the linear dependence between the pressure drop and the stresses in the Darcy flow regime [33]. Voronov *et al.* [37], based on a numerical investigation of flow of an incompressible Newtonian fluid through salt-leached porous scaffolds, have proposed the following empirical correlation for the average stress in the open pore space,

$$\bar{\tau} = (0.0851 \pm 0.0064) \left(\frac{\Delta P}{L} \right)^{0.503 \pm 0.015} U_S^{0.497 \pm 0.015}, \quad (9)$$

where $\Delta P/L$ is the pressure drop and U_S is the superficial velocity. In flow following Darcy's law, $\Delta P/L$ is proportional to the superficial fluid velocity, U_S . Equation (9) then leads to a linear relation between $\bar{\tau}$ and $\Delta P/L$, which is consistent with expectations, for example, with the Wang and Tarbell equation for flow around spheres and cylinders [48,49]. Note also that the constant involved in the expression is proportional to $\sqrt{\eta}$.

Another important consideration is to find a common pdf model that can fit the normalized distributions within statistically acceptable accuracy. Such common pdf models, describing different physical phenomena ranging from the distribution of rain droplet sizes to the distribution of friction coefficients (among others), have been obtained in other cases [50–52]. In order to reveal a common pdf, normalized stress data presented in Fig. 2 were tested with 65 different common pdf models, available in the EASYFIT software, version 5.4 [47]. The goodness-of-fit test between the pdf models and our data was conducted using the (KS) test. The null hypothesis was as follows: “the normalized stress pdf follows the tested pdf model.” The level of significance, α , was chosen to be 0.2. By choosing $a = 0.2$, the acceptance of the null hypothesis is more rigorous than acceptance at the usual choice of $a = 0.05$. Note that, in the KS test, the critical value of the KS statistic decreases when α increases and that the null hypothesis is rejected when the critical value is smaller than that of the test statistic of a data sample. Thus, at a given value of the calculated test statistic, testing for the null hypothesis at a higher α increases the probability of rejecting the null hypothesis. Such a high level of α has been used for testing null hypotheses in other published works [30,53,54]. Table II is a summary of pdf models that best describe the actual dimensional and normalized pdf data along with the KS statistic, the corresponding p values, and the level of significance for rejecting a true null hypothesis. The KS test results in Table II indicate that eight listed pdf models can predict the normalized stress distributions of packed beds with spheres within the prescribed statistical accuracy. Among those listed, the three-parameter γ (3P- γ), the three-parameter log-logistic (3P-log-logistic), and the three-parameter lognormal (3P-lognormal) were found to be also valid for all the dimensional distributions shown in which a true null hypothesis cannot be rejected at $\alpha = 0.2$. The p value for the case of randomly packed spheres is one for these cases.

B. Relation between the pore size and space stress distribution and prediction of the common pdf

At this point one may inquire which one among the three models is the most appropriate to use. One way to answer this question is to explicitly show how the stresses distribute in the pore space through the use of analytical results. The governing equations for creeping flow over an array of spheres are usually obtained in integral form from a transformation of the Navier-Stokes equation [26,55]. Unfortunately, solving these equations is not simple. Instead we draw a connection between the pore size distribution and the stress distribution by utilizing a simplified model of the pore network as a bundle of capillary tubes [56–58]. In brief, we assume that the pore network of an array of spheres can be represented by a bundle of circular straight capillary tubes with different diameters. This simplification has been found to be valuable in studies of flow behavior in unconsolidated porous media [59,60]. Since the pore network is regarded as an ensemble of circular capillary tubes, the stress profile in any one individual tube is found as follows [61]:

$$\tau = \frac{\Delta P}{L} \frac{r}{2}, \quad (10)$$

where τ is the fluid stress and r is the radial distance from the tube center. Statistically, if the pdf of r is known, then knowing the pdf of the dependent variable τ can be calculated from the pdf of r , the inverse function of Eq. (10) and its derivative [62]. According to published reports [63–65], the pore size distribution of soil and some types of ultrafiltration membranes follows the log-normal law. In other words, the pore radius is log-normally distributed and is formulated as

$$f(r) = \frac{\exp\left[-\frac{1}{2}\left(\frac{\ln r - \mu'}{\sigma'}\right)^2\right]}{r\sigma'\sqrt{2\pi}}, \quad (11)$$

where $f(r)$ is the probability density function of the pore radius and μ' and σ' are the continuous parameters of the distribution ($\sigma' > 0$) [the log-normal is denoted by log-normal (μ', σ') for convenience]. Applying the transformation method for Eq. (10), the pdf of the dependent variable, τ , is found as follows [62]:

$$f(\tau) = \frac{\exp\left[-\frac{1}{2}\left(\frac{\ln \tau - \mu}{\sigma}\right)^2\right]}{\tau\sigma\sqrt{2\pi}}, \quad (12)$$

where $\sigma = \sigma'$ and $\mu = \mu' - \ln\left(\frac{2}{\Delta P/L}\right)$. It is obvious from Eq. (12) that the pattern of $f(\tau)$ is identical to that of $f(r)$ in which σ' is unchanged and $\mu = \mu' - \ln\left(\frac{2}{\Delta P/L}\right)$. Consequently, the average stress, $\bar{\tau}$, and the standard deviation, σ_τ , are related to the two continuous parameters of the distribution as [66]

$$\begin{aligned} \bar{\tau} &= e^{\mu + \frac{\sigma^2}{2}} \\ \sigma_\tau &= e^{\mu + \frac{\sigma^2}{2}} \sqrt{e^{\sigma^2} - 1}. \end{aligned} \quad (13)$$

The connection between the pore size distribution and the stress distribution in a porous medium where the pore network is represented as a bundle of capillary tubes is strengthened by an extreme case presented in Appendix A.

It is also important to note here that if the pdf of the dimensional stresses is log-normal (μ, σ), then the pdf of

the normalized stresses, τ^* , is 3P log-normal (γ^* , μ^* , σ) and the pdf can be written as follows:

$$f(\tau^*) = \frac{\exp\left[-\frac{1}{2}\left(\frac{\ln(\tau^* - \gamma^*) - \mu^*}{\sigma}\right)^2\right]}{\sigma\sqrt{2\pi}(\tau^* - \gamma^*)}, \quad (14)$$

where $\gamma^* = -\frac{\bar{\tau}}{\sigma_\tau}$ is the continuous location parameter, $\mu^* = \mu - \ln \sigma_\tau$, and σ remains the same as that of $f(\tau)$. Proof of this result can be obtained with a procedure analogous to the transformation of the normal distribution, $N(\bar{X}, \sigma_X^2)$, of a random variable X to the standard normal distribution, $N(0, 1)$, of the random variable $(X - \bar{X})/\sigma_X$ (see Appendix B) [67]. The above relation of γ^* to $\bar{\tau}$ and σ_τ implies that one can calculate γ^* from the minimum normalized stress value, since the physical interpretation of the location parameter γ^* is that it represents the minimum value of the random variable (the starting point of the normalized stress distribution). This relation along with Eq. (13) yields the relationship between γ^* and σ as follows:

$$\gamma^* = -\frac{1}{\sqrt{e^{\sigma^2} - 1}}. \quad (15)$$

Furthermore, the expression $\mu^* = \mu - \ln \sigma_\tau$ leads to the relation of μ^* and σ , as follows:

$$\mu^* = -\frac{\sigma^2}{2} - \ln \sqrt{e^{\sigma^2} - 1}. \quad (16)$$

Therefore, when γ^* is known, the parameters of the log-normal (γ^* , μ^* , σ) can be predicted. However, it is somewhat difficult to analytically estimate the value of γ^* , since the flow conditions and the pore structure exert strong influences on $\bar{\tau}$ and σ_τ . Our simulation data can be used to obtain the value of γ^* from the minimum normalized stresses, τ_{\min}^* , of the normalized stress distributions. It is seen in Fig. 2 that τ_{\min}^* for all the packing morphologies is approximately -2 or $\gamma^* = -2$. Subsequently, σ and μ^* can be calculated from Eqs. (15) and (16), leading to the result that the common distribution of the normalized stresses is the log-normal $(-2, 0.588, 0.47)$. The predicted log-normal $(-2, 0.588, 0.47)$ is depicted in Fig. 3 with the normalized stress distributions in the open space of four examined sphere packing geometries. The agreement is apparent with the naked eye without the aid of statistical analysis in the case of fcc and randomly packed spheres.

C. Validity of the predicted log-normal pdf in porous scaffold structures

The above considerations suggest that the 3P log-normal $(-2, 0.588, 0.47)$ might be a good approximation for the stress distributions in the open space of packed-sphere beds under Darcy flow conditions. In order to examine whether this finding holds for other cases of porous media, stress distributions in the pore space of highly porous scaffolds were examined next. A finite volume-based numerical method (available in the commercial computational fluid dynamics software FLUENT, version 12.0.12), was used as an alternative approach to the LBM for the simulation of the flow. Six different porous scaffold geometries were simulated, such as those that can be fabricated by rapid prototyping techniques. The porosity was chosen to be 85%, in the range often used in scaffolds (see Fig. 4) [45]. The physical properties of the fluid were the same as those for the packed bed cases simulated with

LBM. The flow was periodic in the X , Y , and Z directions. The details of these simulations, the computational mesh size generation, and the stresses on the surface of the solid structure elements of these scaffolds have been discussed in Ref. [45]. The fluid stresses in the open pore space for these geometries were also normalized by applying Eq. (8). The normalized stress distributions of all examined scaffold geometries are illustrated in Fig. 5 along with the 3P log-normal $(-2, 0.588, 0.47)$ distribution. Despite different geometric morphologies, the normalized stress distributions exhibit similar features, such as positive skewness, the same peak position, and single mode. Within six scaffold geometries, the agreement of the normalized stress distribution of structures A, B, C, D, and E with the 3P log-normal $(-2, 0.588, 0.47)$ law was confirmed by the KS test, when the null hypothesis cannot be rejected at $\alpha = 0.2$ (p values were 0.21, 0.26, 0.32, 0.66, and 0.35 for structures A, B, C, D, and E, respectively). For case F, the level of significance to accept the null hypothesis is $\alpha = 0.1$ (p value = 0.14).

D. Validity of the predicted log-normal law in Berea sandstone and obtainment of log-normal law of dimensional bulk stress distributions

When the normalized stress distribution of a certain porous medium follows the log-normal $(-2, 0.588, 0.47)$, it is straightforward to find the log-normal (μ, σ) of the dimensional stresses as follows [see Eq. (16) and related comments]:

$$\begin{aligned} \mu &= 0.588 + \ln \frac{\bar{\tau}}{2} \\ \sigma &= 0.47. \end{aligned} \quad (17)$$

So long as $\bar{\tau}$ is unknown, the dimensional stress distribution of the porous medium remains unpredicted. To address this issue, Darcy's law is rearranged to solve for $\Delta P/L$, and then substituted into Eq. (9) to obtain the following expression [note that the constant in Eq. (9) is considered to be $B\sqrt{\eta}$]:

$$\bar{\tau} = B \frac{\eta}{\sqrt{k}} U_S, \quad (18)$$

where k is the permeability of the porous medium. It is noted that the form of Eq. (18) is identical to the Wang and Tarbell equation, in which the average shear stress for flow around a periodic square array of cylinders is estimated [47]. In that equation, B is the constant characterizing the porous medium, i.e., $B = 4/\pi$ for an array of cylinders. The B value for the porous media considered in this study was found by fitting $\bar{\tau}$, computed from simulation data, to a linear function of $\frac{\eta}{\sqrt{k}} U_S$. The slope of the trend line turned out to be 1.41 with a coefficient of determination $R^2 = 0.997$ for beds packed with spheres, and it was found to be 0.526 with $R^2 = 0.9$ for highly porous scaffolds. Thus far, since the correlation for predicting the average stress has been revealed, the dimensional stress distribution of a porous medium, for which the normalized stress distribution follows the 3P log-normal law suggested above, is predicted to be log-normal $[0.588 + \ln(B \frac{\eta}{2\sqrt{k}} U_S), 0.47]$.

Finally, the dimensional stress distribution and the corresponding normalized stress distribution in the pore spaces of a consolidated Berea sandstone slab were determined

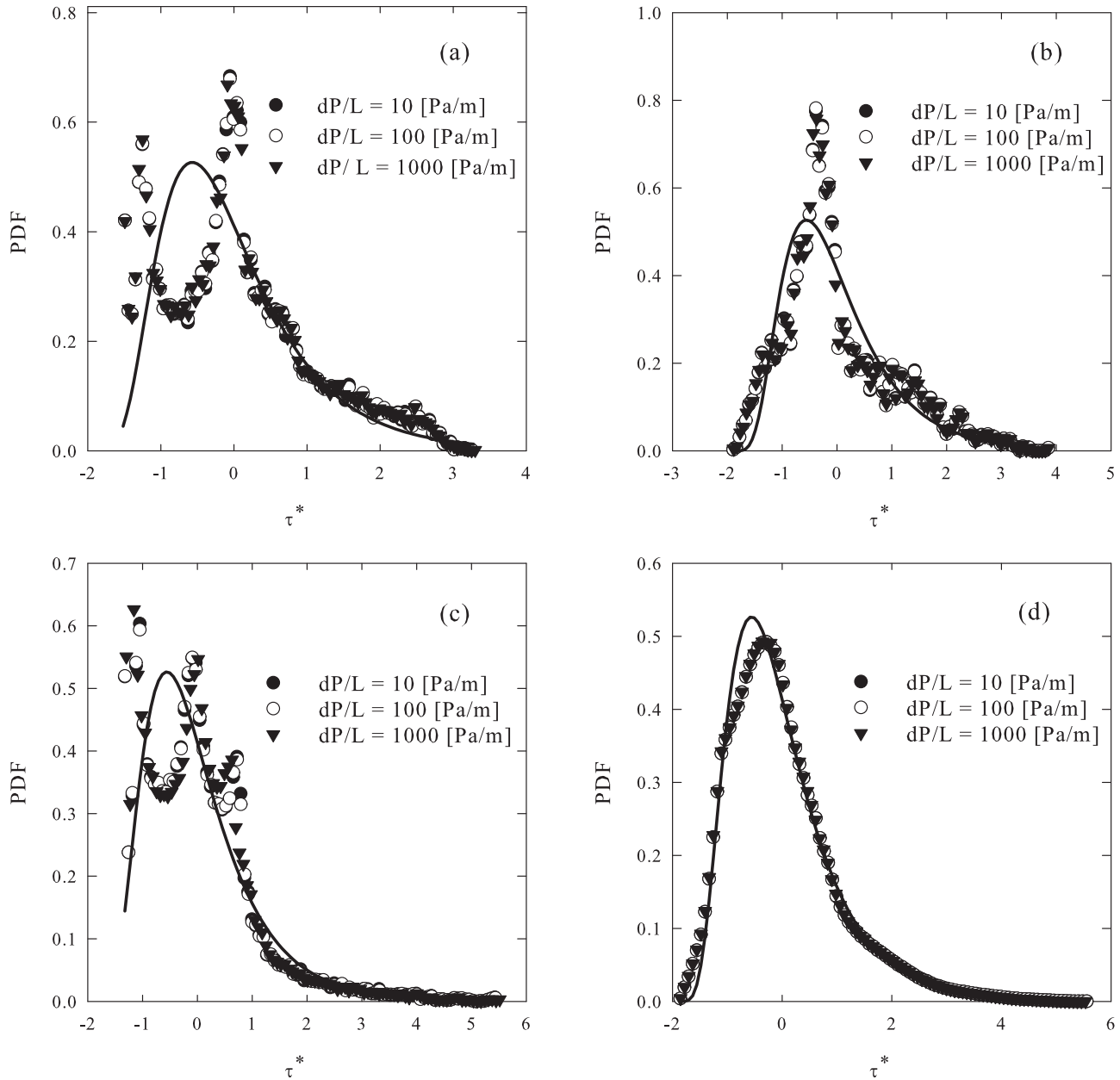


FIG. 3. Normalized stress data in Fig. 2 along with the three parameter log-normal distribution (solid line). The goodness of fit was tested using the Kolgomorov-Smirnov test. Spheres are packed in (a) bcc, (b) fcc, (c) sc, and (d) random configurations.

and fit to the log-normal $[0.588 + \ln(B \frac{\eta}{2\sqrt{k}} U_S), 0.47]$ and log-normal $(-2, 0.588, 0.47)$, respectively. In this case, $B = 1.41$ was employed. The 3D geometry of the sandstone was reconstructed from its 2D grayscale images, obtained after scanning the rock sample by a micro-CT machine (X-Radia, $4.5 \mu\text{m}$ resolution). A 2D image analysis was also applied to the pore size distribution. Afterwards, the 3D rock sample was meshed into 16 000 000 grid points using a structured mesh. The low permeability, high tortuosity, and randomness of the pore space of the rock are factors that challenge the validity of the two proposed log-normal laws (see Table I for physical properties of the examined rock). To obtain the stress distributions, the stress field was computed using the LBM simulation after forcing water to flow through the rock sample at a pressure gradient of 10 000 Pa/m.

In contrast to the case of sphere-packed beds as well as highly porous scaffolds, the normalized stress distribution in the pore spaces of the consolidated Berea sandstone shows a completely different behavior. The values of the pdf of finding a certain range of stresses dramatically decreases over the whole range of normalized stress, from the smallest to the largest value, and no peak is recognized. It is more likely that the stress distribution computed from the simulation of the Berea rock sample follows the exponential distribution rather than the 3P log-normal distribution (data not shown).

The finding that high pdf frequency values correspond to low stresses in sandstone can be physically interpreted by the existence and dominance of flow regions with velocities that are very slow or even in the negative flow direction. This is expected, since common Berea sandstones exhibit highly

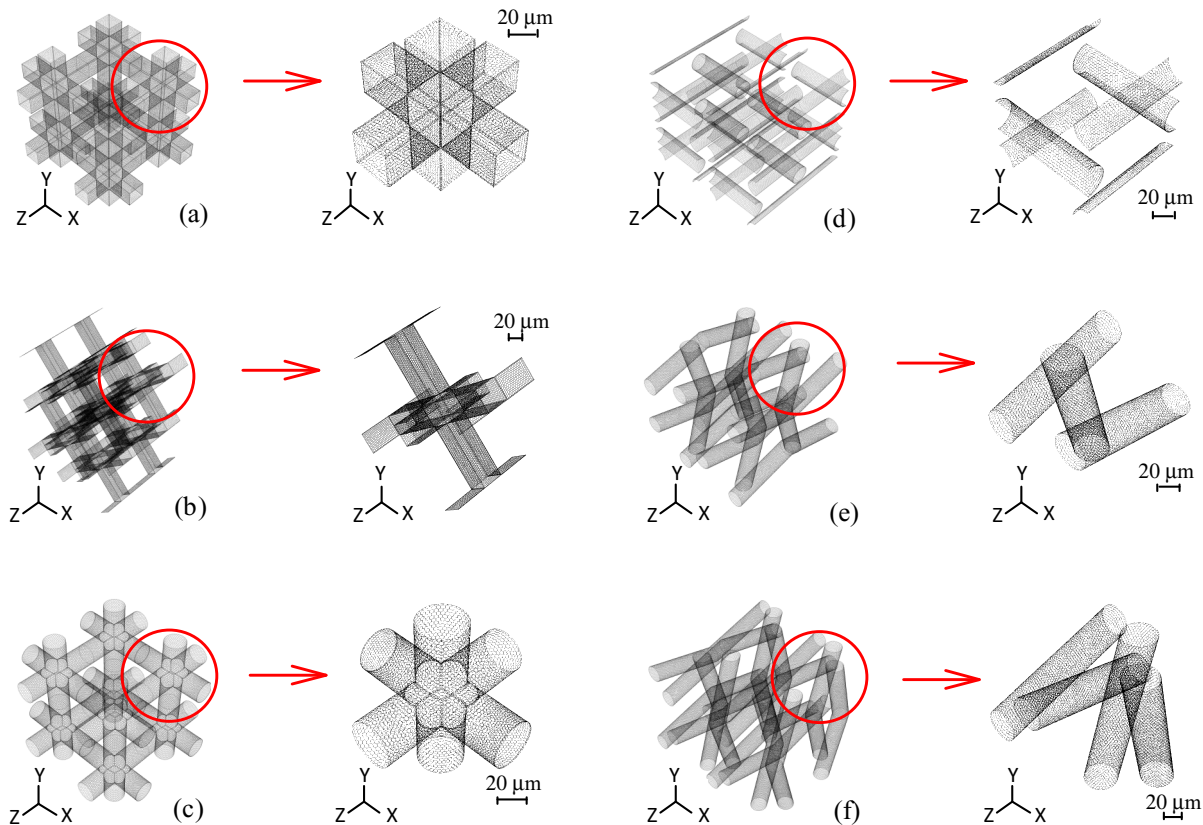


FIG. 4. (Color online) Structure of different porous scaffolds with polyhedral mesh. Simulations were conducted based on single periodic units, presented in magnification in the panel to the right for each case. (Figure adapted from Ref. [45].)

tortuous pore networks that can create pockets of fluid with circulation patterns and flow retardation. However, the motion of nanoparticles injected into the empty space of the rock will not be significantly affected by those regions, since the particles would tend to follow streamlines that guide them to the outlet. Such behavior was affirmed by conducting tracer particle simulations in the Lagrangian framework (not presented herein). Briefly, after the velocity field was computed

by the lattice Boltzmann simulation, a set of conservative tracers was injected into the pore space of the examined Berea sandstone sample using the technique described in Ref. [36]. The results of these simulations indicate that the tracer particles follow the streamlines guiding them to the outlet of the porous domain rather than entering low velocity regions within the pore network. Such low-velocity regions include negative and near-zero velocities that can dramatically delay the particle effluent time. It is then reasonable to reconstruct the stress distribution after filtering out stresses caused by negative velocities. The reconstructed stress distribution of the examined Berea sandstone in dimensionless and dimensional form is depicted in Figs. 6(a) and 6(b), respectively. Note that the stresses over 0.15 Pa are not included in these distributions, since the probability of finding stresses above that value is extremely low, and thus they are neglected. The KS test results with the null hypothesis as follows: “the actual pdf follows the 3P log-normal (−2, 0.588, 0.47) distribution” indicated that the null hypothesis cannot be rejected at $\alpha = 0.2$ (p value = 0.92).

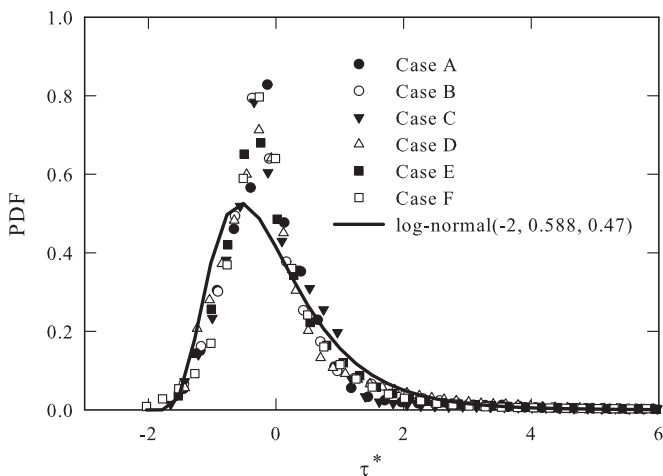


FIG. 5. Normalized stress distributions in the pore space of six different porous scaffolds along with the common three parameter log-normal distribution.

It should be noted that this pdf form is found to be similar to the shape of the pore size distribution for the Berea sandstone presented as an inset in Fig. 6(a). As was also found using the model of a bundle of capillary tubes, there is a theoretical connection between the pore size distribution and the stress distribution in the pore spaces of a porous medium. The prediction for the dimensional stresses is log-normal (−3.92, 0.47), obtained by plugging k and U_s into the predictive

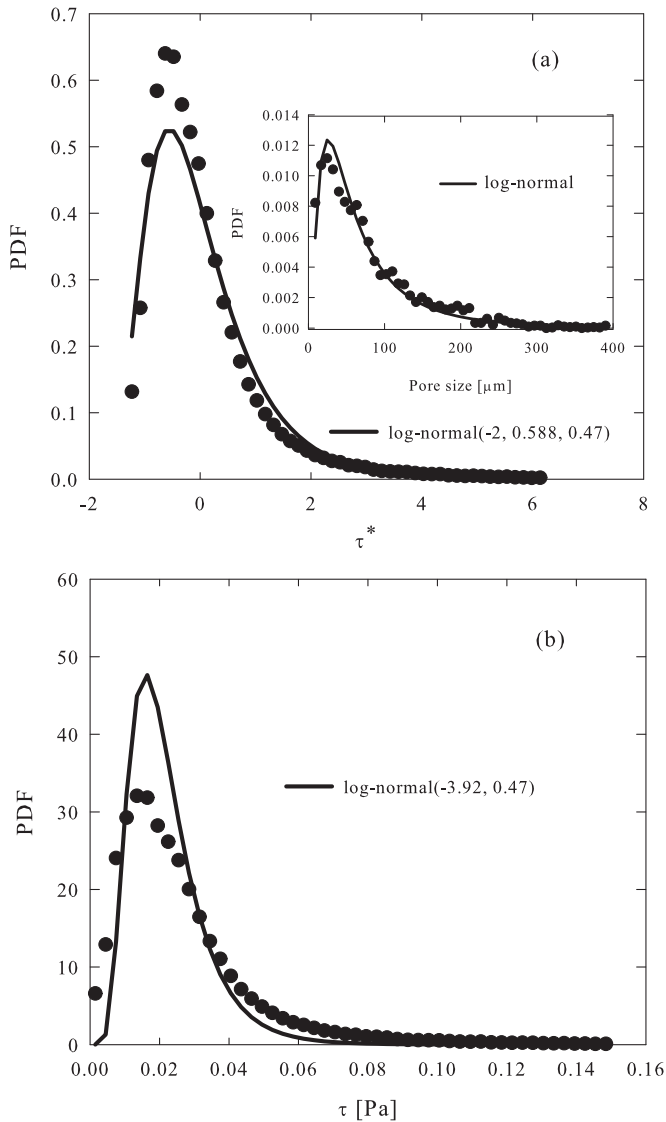


FIG. 6. Stress distribution in the pore space of a $0.92 \times 1.8 \text{ mm}^3$ Berea sandstone slab in dimensional and dimensionless form. (a) Normalized stress distribution in association with the common 3P log-normal. The inset illustrates the pore size distribution of the Berea slab. (b) Dimensional stress distribution along with its prediction, computed from the log-normal $[0.588 + \ln(B \frac{\eta}{2\sqrt{k}} U_S), 0.47]$.

formula, i.e., the log-normal $[0.588 + \ln(B \frac{\eta}{2\sqrt{k}} U_S), 0.47]$ with $B = 1.41$, and is presented in Fig. 6(b). (See Table I for the permeability of the Berea slab and other geometries.) It is apparent from Fig. 6(b) that the acceptance of the null hypothesis [“the dimensional pdf follows the predicted log-normal $(-3.92, 0.47)$ ” at $\alpha = 0.2$] implies that the predicted stress distribution holds even for structures with low porosity and a sophisticated pore network like in Berea sandstone. While Fig. 6(b) is a presentation of the same data as in Fig. 6(a) in dimensional form, Fig. 6(b) provides a visual assessment as to how well the predicted 2P log-normal fits to the dimensional stress data. It is also apparent from Fig. 6(b) that further considerations are needed to determine the value of the geometric factor B for the reservoir-rock-type geometries.

IV. CONCLUSIONS

Stress distributions in the open space of ideally and randomly packed beds with spheres were numerically computed in this work. It was found that the distribution is unimodal when the beds were fcc and randomly packed, whereas it is bimodal and trimodal in the case of bcc and sc spheres, respectively. For each particular sphere packing morphology, the distribution pattern remains unchanged for different pressure drops but under Darcy flow conditions. Additionally, the KS goodness of fit test results indicate that the 3P log-normal distribution can be used to describe the normalized stress distribution computed for randomly packed spheres and fcc-packed spheres. A common 3P log-normal distribution exhibits agreement with the stress data within statistical accuracy. Likewise, normalized stress distributions of other cases of highly porous structured scaffolds are also found to considerably agree with the predicted 3P log-normal distribution. In addition, a similarity between the pore size distribution and the associated normalized stress distribution is observed when simulating flow in the pore space of the Berea sandstone geometry. Therefore, one can infer that the pore size distribution of a porous medium profoundly affects the distribution of the fluid stresses in the void spaces. Findings from this work can be useful in predicting the pdf of stresses that nano- and microparticles encounter as they travel through different types of porous media and in predicting the stability of these particles.

APPENDIX A: CONNECTION BETWEEN PORE SIZE AND DIMENSIONAL BULK STRESS DISTRIBUTION IN A PORE NETWORK ASSUMED AS A BUNDLE OF CAPILLARY TUBES

Consider a porous medium with circular, straight tubelike pores. Let the diameter of the pores, D , take values from an arithmetic sequence between 1 and $50 \mu\text{m}$ (i.e., each diameter is larger than the one smaller than itself by $\Delta D = 1 \mu\text{m}$) and let us assume that the diameters follow a log-normal

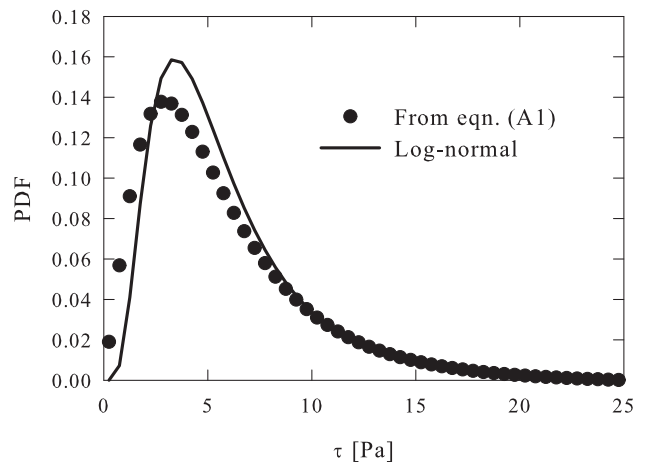


FIG. 7. Stress distribution in a porous medium modeled by a bundle of circular capillary tubes with different diameters. The pressure difference across the medium is $1 \text{ Pa}/\mu\text{m}$. The log-normal $(1.6, 0.61)$ distribution is presented by the black solid line.

TABLE I. Geometric characteristic of examined porous media.

Geometry	Domain size (μm^3)	Porosity (%)	Permeability (m^2)	Size of structural element ^a (μm)
fcc spheres	1414.2 ³	25.95	1.848×10^{-10}	1000
bcc spheres	1143.3 ³	31.98	5.226×10^{-10}	1000
Randomly packed spheres	2000 ³	39.76	1.116×10^{-9}	1000
sc spheres	1000 ³	47.64	2.841×10^{-9}	1000
Case (a)	143.2 ³	85	3.701×10^{-10}	35
Case (b)	$202.5^2 \times 143.2$	85	3.606×10^{-10}	35
Case (c)	127 ³	85	3.174×10^{-10}	35
Case (d)	113.26 ³	85	2.315×10^{-10}	35
Case (e)	141.14 ³	85	3.608×10^{-10}	35
Case (f)	162.97 ³	85	3.848×10^{-10}	35
Berea slab	$900^2 \times 1800$	20.08	2.428×10^{-12}	—

^aThe structural element is the sphere diameter in sphere-packing cases, the cylinder diameter in Cases (c)–(f), and the edge of the bar cross section in Cases (a) and (b).

distribution. Fluid is driven through these parallel tubes by a pressure difference of $1 \text{ Pa}/\mu\text{m}$. Recall that the stress profile in each pore is linearly correlated to the pore diameter as described in Eq. (10). In order to estimate the distribution of stresses in each pore, bins of stresses are created with each bin interval chosen to be 0.01 Pa ($\Delta\tau = 0.01 \text{ Pa}$). Given the above, in each pore the number of stress bins depends on the pore diameter, so there are 50 bins in a pore with $D = 1$ and 100, 150 . . . , 2500 stress bins in pores of diameter $D = 2, 3 \dots, 50 \mu\text{m}$, respectively. Because the pore diameter follows the log-normal distribution, the probability of finding a stress bin in a particular pore is proportional to the probability of finding that pore in the network. As a result, the *global* frequency of finding a stress bin in the pore network is a summation of the *local* frequency of finding a bin with similar stress values in each one of the pores that follow the log-normal distribution.

This summation can be mathematically stated as

$$f(\tau) = \sum_{i=1}^{50} f_i(\tau) \times f_r(D_i) \quad (\text{A1})$$

where $f(\tau)$ is the *global* frequency of finding a stress in the network, $f_i(\tau)$ is the *local* frequency finding a stress in a pore with diameter D_i and $f_r(D_i)$ is the frequency of finding pores in the network with diameter equal to D_i . By doing so, the pdf of the *global* stress can be calculated, and the shape of the pdf curve can be seen in Fig. 7. It is evident from Fig. 7 that the pdf follows the log-normal pattern, presented by the black solid line. The fact that the null hypothesis cannot be rejected at $\alpha = 0.2$ after testing by the Kolmogorov-Smirnov test indicates that the stresses in this particular bundle of tubes follows the log-normal law.

TABLE II. Results from the Kolmogorov-Smirnov goodness-of-fit test for 8 among 65 pdf models. Values obtained from one pressure drop ($dP/L = 10 \text{ Pa/m}$) are presented, as statistics of other cases do not change significantly, because of the linearity between stress and pressure drop in the examined range. The p values are also shown in parentheses. Note that the values of the critical Kolmogorov-Smirnov statistic for $\alpha = 0.05$ and $\alpha = 0.2$ are 0.1340 and 0.1056, respectively. We accept the null hypothesis when the KS statistic is smaller than the critical value for the respective level of significance.

pdf model	Kolmogorov-Smirnov statistic value (p value)							
	Normalized stress				Dimensional stress			
	bcc	fcc	sc	Random	bcc	fcc	sc	Random
4P-Burr	0.0792 (0.53)	0.0752 (0.59)	0.0748 (0.60)	0.0218 (1.0)	0.0696 (0.70)	0.0764 (0.58)	0.2444 (9.7×10^{-6})	0.0739 (0.62)
3P-Fatigue life	0.0755 (0.59)	0.0736 (0.62)	0.0753 (0.59)	0.0273 (1.0)	0.0754 (0.59)	0.1208 (0.099)	0.0753 (0.59)	0.0273 (1.0)
3P- γ	0.0909 (0.36)	0.0781 (0.55)	0.0839 (0.46)	0.0331 (1.0)	0.0909 (0.36)	0.0782 (0.55)	0.0838 (0.46)	0.0332 (1.0)
3P-Inverse Gaussian	0.0734 (0.63)	0.0733 (0.63)	0.0731 (0.63)	0.0273 (1.0)	0.2161 (1.4×10^{-4})	0.1204 (0.101)	0.0727 (0.64)	0.0889 (0.38)
3P-Log-logistic	0.0659 (0.75)	0.0583 (0.86)	0.0667 (0.74)	0.0297 (1.0)	0.0659 (0.75)	0.0585 (0.86)	0.0667 (0.74)	0.0298 (1.0)
3P-Lognormal	0.0693 (0.70)	0.0719 (0.65)	0.0703 (0.68)	0.0268 (1.0)	0.0693 (0.69)	0.0721 (0.65)	0.0703 (0.68)	0.0269 (1.0)
3P-Pearson type 5	0.0642 (0.78)	0.0705 (0.67)	0.0648 (0.77)	0.0261 (1.0)	0.2087 (2.7×10^{-4})	0.1504 (0.019)	0.1703 (5.2×10^{-3})	0.1148 (0.13)
4P-Pearson type 6	0.0726 (0.64)	0.0710 (0.67)	0.0762 (0.58)	0.0266 (1.0)	0.0852 (0.44)	0.0764 (0.58)	0.0745 (0.61)	0.2818 (1.7×10^{-7})

APPENDIX B: LOG-NORMAL (γ^* , μ^* , σ) OF τ^* AS A CONSEQUENCE OF LOG-NORMAL (μ , σ) OF τ

If τ is lognormal(μ , σ), what is $\tau^* = \frac{\tau - \bar{\tau}}{\sigma_\tau}$?

Cumulative pdf: $G(z) = P(\tau^* \leq z) = P(\frac{\tau - \bar{\tau}}{\sigma_\tau} \leq z) = P(\tau \leq z\sigma_\tau + \bar{\tau})$ So,

$$G(z) = \int_0^{z\sigma_\tau + \bar{\tau}} \frac{1}{\sigma_\tau \sqrt{2\pi}} \exp\left[-\frac{(\ln \tau - \mu)^2}{2\sigma^2}\right] d\tau. \quad (B1)$$

But

$$\frac{d\tau}{d\tau^*} = \sigma_\tau \Rightarrow d\tau = \sigma_\tau d\tau^*. \quad (B2)$$

We also have the following:

$$\begin{aligned} \ln \tau - \mu &= \ln(\tau^* \sigma_\tau + \bar{\tau}) - \mu = \ln\left[\sigma_\tau\left(\tau^* + \frac{\bar{\tau}}{\sigma_\tau}\right)\right] - \mu \\ &= \ln\left(\tau^* + \frac{\bar{\tau}}{\sigma_\tau}\right) - (\mu - \ln \sigma_\tau). \end{aligned} \quad (B3)$$

Substituting (B2) and (B3) into (B1), we obtain

$$\begin{aligned} G(z) &= \int_0^z \frac{1}{\sigma_\tau (\tau^* + \frac{\bar{\tau}}{\sigma_\tau}) \sigma \sqrt{2\pi}} \\ &\quad \times \exp\left[-\frac{\left[\ln\left(\tau^* + \frac{\bar{\tau}}{\sigma_\tau}\right) - (\mu - \ln \sigma_\tau)\right]^2}{2\sigma^2}\right] \sigma_\tau d\tau^*. \end{aligned}$$

So τ^* is lognormal(γ^* , μ^* , σ), where $\gamma^* = -\frac{\bar{\tau}}{\sigma_\tau}$ and $\mu^* = \mu - \ln \sigma_\tau$.

APPENDIX C: PORE SIZE DISTRIBUTIONS OF FCC PACKING, BCC PACKING, SC PACKING, AND RANDOM PACKING SPHERES

Pore size distributions of four sphere packing geometries are presented in Fig. 8.

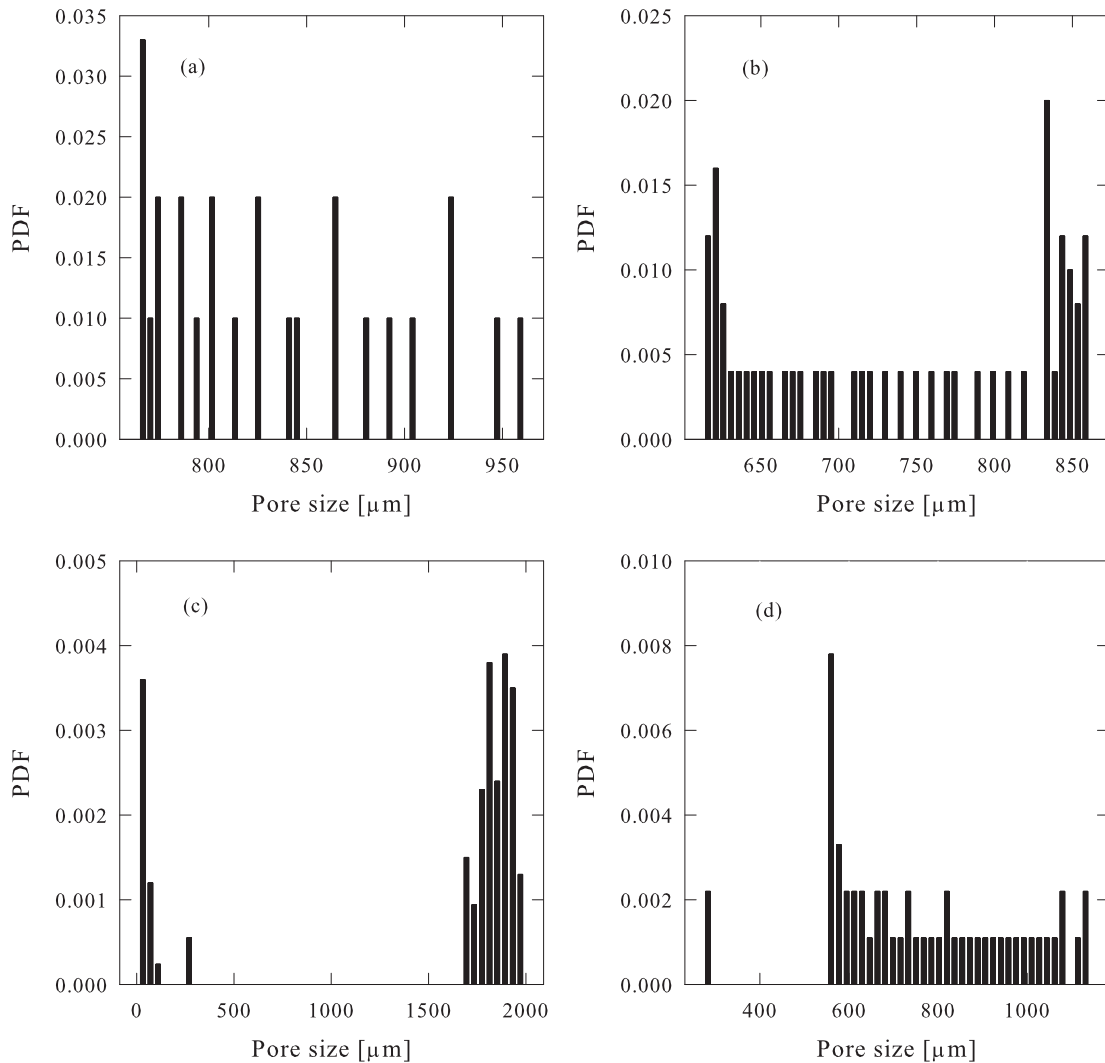


FIG. 8. Pore size distributions of the studied sphere packing patterns. Spheres are packed in (a) fcc, (b) bcc, (c) random, and (d) sc random configurations.

- [1] S. H. Cartmell, B. D. Porter, A. J. Garcia, and R. E. Gulberg, *Tissue Eng.* **9**, 1197 (2003).
- [2] J. F. Alvarez-Barreto, S. M. Linehan, R. L. Shambaugh, and V. I. Sikavitsas, *Ann. Biomed. Eng.* **35**, 429 (2007).
- [3] J. F. Alvarez-Barreto and V. I. Sikavitsas, *Macromol. Biosci.* **7**, 579 (2007).
- [4] H. Inoguchi, T. Tanaka, Y. Maehara, and T. Matsuda, *Biomaterials* **28**, 486 (2007).
- [5] J. D. Fortner, D. Y. Lyon, C. M. Sayes, A. M. Boyd, J. C. Falkner, E. M. Hotze, L. B. Alemany, Y. J. Tao, W. Guo, K. D. Ausman, V. L. Colvin, and J. B. Hughes, *Environ. Sci. Technol.* **39**, 4307 (2005).
- [6] E. Oberdörster, *Environ. Health Perspect.* **112**, 1058 (2004).
- [7] C. M. Sayes, A. M. Gobin, K. D. Ausman, J. Mendez, J. L. West, and V. L. Colvin, *Biomaterials* **26**, 7587 (2005).
- [8] A. L. Alpatova, W. Shan, P. Babica, B. L. Upham, A. R. Rogensues, S. J. Masten, E. Drown, A. K. Mohanty, E. C. Alcolilja, and V. V. Tarabara, *Water Res.* **44**, 505 (2010).
- [9] J. Gao, S. Youn, A. Hovsepyan, V. L. Llana, Y. Wang, G. Bitton, and J. J. Bonzongo, *Environ. Sci. Technol.* **43**, 3322 (2009).
- [10] M. Bottini, S. Bruckner, K. Nika, N. Bottini, S. Bellucci, A. Magrini, A. Bergamaschi, and T. Mustelin, *Toxicol. Lett.* **160**, 121 (2006).
- [11] A. J. Kennedy, M. S. Hull, J. A. Stevens, K. M. Dontsova, M. A. Chappell, J. C. Gunter, and C. A. Weiss, *Environ. Toxicol. Chem.* **27**, 1932 (2008).
- [12] M. M. Saggaf and S. Aramco, *J. Petrol. Technol.* **60**, 54 (2008).
- [13] A. S. Stordal and D. S. Oliver, *Adv. Water Resour.* **34**, 946 (2011).
- [14] J. Ullo, *Sci. Model. Simul.* **15**, 313 (2008).
- [15] M. S. Zaman, M. R. Islam, and S. Mokhatab, *Petrol. Sci. Technol.* **30**, 1053 (2012).
- [16] L. C. Villamizar, P. Lohateeraparp, J. H. Harwell, D. E. Resasco, and B. J. Shiau, *Transport Porous Med.* **96**, 63 (2013).
- [17] M. R. Rojas, A. J. Müller, and A. E. Sáezb, *J. Colloid Interface Sci.* **326**, 221 (2008).
- [18] M. Vasudevan, E. Buse, D. Lu, H. Krishna, R. Kalyanaraman, A. Q. Shen, B. Khomami, and R. Sureshkumar, *Nature* **9**, 436 (2010).
- [19] W. R. Schowalter, *Adv. Colloid Interface Sci.* **17**, 129 (1982).
- [20] H. S. Chung and R. Hogg, *Colloids Surf.* **15**, 119 (1985).
- [21] G. R. Zeichner and W. R. Schowalter, *J. Colloid Interface Sci.* **71**, 237 (1979).
- [22] W. R. Schowalter, *Annu. Rev. Fluid Mech.* **16**, 245 (1984).
- [23] M. Bäbler, M. Morbidelli, and J. Baldyga, *J. Fluid Mech.* **612**, 261 (2008).
- [24] Y. Jia, L. An, and R. K. Wang, *J. Biomed. Opt.* **14**, 050504 (2009).
- [25] G. Grossman, *AIChE J.* **21**, 720 (1975).
- [26] A. A. Zick and G. M. Homsy, *J. Fluid Mech.* **115**, 13 (1982).
- [27] D. Mertens, C. Heinen, E. H. Hardy, and H. W. Buggisch, *Chem. Eng. Technol.* **29**, 854 (2006).
- [28] S. Sarkar and G. S. Gupta, *Metall. Mater. Trans. B* **38**, 965 (2007).
- [29] A. K. Jaiswal, T. Sundararajan, and R. P. Chhabra, *Int. J. Eng. Sci.* **29**, 693 (1991).
- [30] R. S. Voronov, S. B. VanGordon, V. I. Sikavitsas, and D. V. Papavassiliou, *Appl. Phys. Lett.* **97**, 024101 (2010).
- [31] R. A. Gutierrez and E. T. Crumpler, *Ann. Biomed. Eng.* **36**, 77 (2008).
- [32] A. Lesman, Y. Blinder, and S. Levenberg, *Biotechnol. Bioeng.* **105**, 645 (2010).
- [33] M. Campolo, F. Curcio, and A. Soldati, *AIChE J.* **59**, 3131 (2013).
- [34] M. C. Sukop and D. T. Thorne, *Lattice Boltzmann Modeling: An Introduction for Geoscientists and Engineers*, 1st ed. (Springer, New York, 2006).
- [35] S. Chen and G. D. Doolen, *Annu. Rev. Fluid Mech.* **30**, 329 (1998).
- [36] R. S. Voronov, S. B. VanGordon, V. I. Sikavitsas, and D. V. Papavassiliou, *Int. J. Numer. Meth. Fluids* **67**, 501 (2010).
- [37] R. S. Voronov, S. B. VanGordon, V. I. Sikavitsas, and D. V. Papavassiliou, *J. Biomech.* **43**, 1279 (2010).
- [38] M. Skoge, A. Donev, F. H. Stillinger, and S. Torquato, *Phys. Rev. E* **74**, 041127 (2006).
- [39] C. A. Chung, C. W. Chen, C. P. Chen, and C. S. Tseng, *Biotechnol. Bioeng.* **97**, 1603 (2007).
- [40] W. L. Grayson, S. Bhumiratana, C. Cannizzaro, P. H. G. Chao, D. P. Lennon, A. I. Caplan, and G. V. Novakovic, *Tissue Eng. Part A* **14**, 1809 (2008).
- [41] M. A. Hussein and T. Becker, *Microfluid. Nanofluidics* **8**, 665 (2010).
- [42] V. I. Sikavitsas, G. N. Bancroft, H. L. Holtorf, J. A. Jansen, and A. G. Mikos, *PNAS* **100**, 14683 (2003).
- [43] S. J. Hollister, *Adv. Mater. (Weinheim, Ger.)* **21**, 3330 (2009).
- [44] S. Yang, K. Faileong, Z. Du, and C. K. Chua, *Tissue Eng.* **8**, 1 (2002).
- [45] N. H. Pham, R. S. Voronov, S. B. VanGordon, V. I. Sikavitsas, and D. V. Papavassiliou, *Biorheology* **49**, 235 (2012).
- [46] B. Porter, R. Zuel, H. Stockman, R. Gulberg, and D. Fyhrle, *J. Biomech.* **38**, 543 (2005).
- [47] <http://www.mathwave.com>.
- [48] D. M. Wang and J. M. Tarbell, *J. Biomech. Eng.* **117**, 358 (1995).
- [49] S. Wang and J. M. Tarbell, *Arterioscler. Thromb. Vasc. Biol.* **20**, 2220 (2000).
- [50] C. Steele, *Reliab. Eng. Syst. Safe.* **93**, 1574 (2008).
- [51] Y. Yaw and R. S. Muller, *Solid State Electron.* **32**, 541 (1989).
- [52] E. Villermaux and B. Bossa, *Nat. Phys.* **5**, 697 (2009).
- [53] S. Harrison, D. D. Murphy, and P. R. Ehrlich, *Am. Nat.* **132**, 360 (1988).
- [54] F. D. Meyer and C. Capel-Boute, *Int. J. Biometeorol.* **31**, 301 (1987).
- [55] H. Hasimoto, *J. Fluid Mech.* **5**, 317 (1959).
- [56] R. M. Griffith, *Chem. Eng. Sci.* **20**, 1015 (1965).
- [57] F. A. L. Dullien, *Porous Media Fluid Transport and Pore Structure*, 2nd ed. (Academic Press, San Diego, 1992).
- [58] E. F. Blick, *Ind. Eng. Chem. Proc. Des. Dev.* **5**, 90 (1966).
- [59] F. C. Blake, *Trans. Am. Inst. Chem. Eng.* **14**, 415 (1922).
- [60] G. M. Fair and L. P. Hatch, *J. Am. Water Works Assoc.* **25**, 1551 (1933).

- [61] R. B. Bird, W. E. Stewart, and E. N. Lightfoot, *Transport Phenomena*, 2nd ed. (John Wiley & Sons, New York, 2002).
- [62] K. M. Ramachandran and C. P. Tsokos, *Mathematical Statistics with Applications*, 1st ed. (Academic Press, San Diego, 2009).
- [63] E. H. D'Hollander, [Water Resour. Res.](#) **15**, 107 (1979).
- [64] K. Kosugi, [Water Resour. Res.](#) **32**, 2697 (1996).
- [65] L. Zeman and G. Tkacik, in *Materials Science of Synthetic Membranes*, edited by D. R. Lloyd (Millipore Corporation, Bedford, 1985), p. 339.
- [66] W. R. Ott, *Environmental Statistics and Data Analysis* (Lewis, Boca Raton, 1995).
- [67] R. V. Hogg and E. A. Tanis, *Probability and Statistical Inference*, 3rd ed. (Macmillan, New York, 1988).